

Electronic Supporting Information

A smart switchable module for detection of multiple-ions *via* turn-on dual-optical readout and their cell-imaging studies

Abhishek Rai^{‡a}, Alok Kumar Singh^{‡b}, Avinash kumar Sonkar,^a Anand Prakash^c,
Jagat Kumar Roy^c, Rajamani Nagarajan^{*b} and Lallan Mishra^{*a}

^aDepartment of Chemistry, Banaras Hindu University, Varanasi, India.

^bDepartment of Chemistry, University of Delhi, Delhi-110 007, India.

^cDepartment of Zoology, Banaras Hindu University, Varanasi, India.

E-mail:lmishrabhu2@gmail.com

[‡]These authors contributed equally to this work.

Cell culture

HeLa is a cervical cancer cell line used for our study. Cells were grown in Dulbecco's modified Eagle's medium (DMEM, HiMedia) supplemented with 10% fetal bovine serum (Invitrogen), and 1X antibiotic cocktail (HiMedia) in a 5% CO₂ incubator at 37°C. Cells were initially kept in 25 cm² culture flask as a stock. For experiment cells were washed with 1X PBS and trypsinised to seed in six well plate as per the experimentation set up.

Cellular imaging methodology

Overnight grown 60-80 % confluent cells were used for experiment. Trypsinised 1x 10⁵ HeLa cells were seeded in six well plate having cover slide in each well and allowed to grow in complete media(prepared in DMEM with 10% FBS and 1X antibiotic cocktail added) overnight in a 5% CO₂ incubator at 37 C. after 24h of incubation cells were washed with 1X PBS, **RHTH** added in media and maintained at 10 μM concentration in solution and incubated for 30 min in 5% CO₂ incubator at 37 C followed by addition of Fe and Hg of concentration of 100 μM for 1 h. For cell imaging study LSM510-Meta software were used.

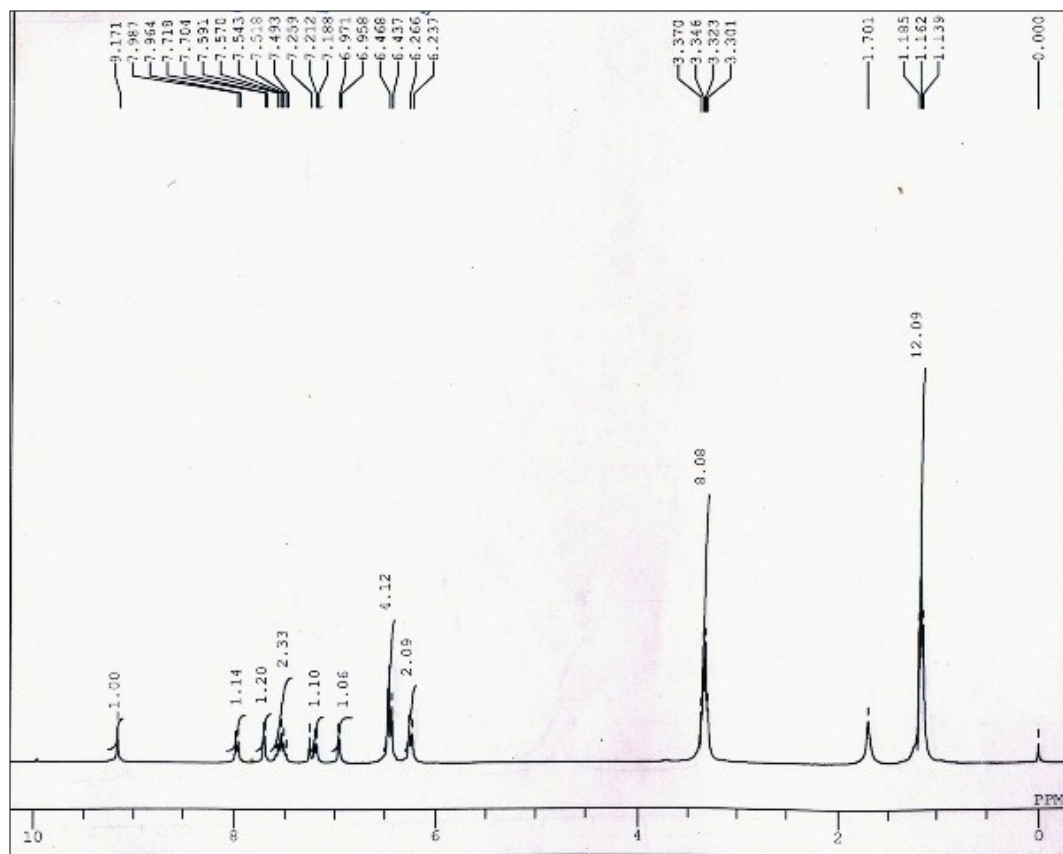


Fig. S1: ¹H-NMR spectrum of **RHTH** in CDCl₃ at room temperature.

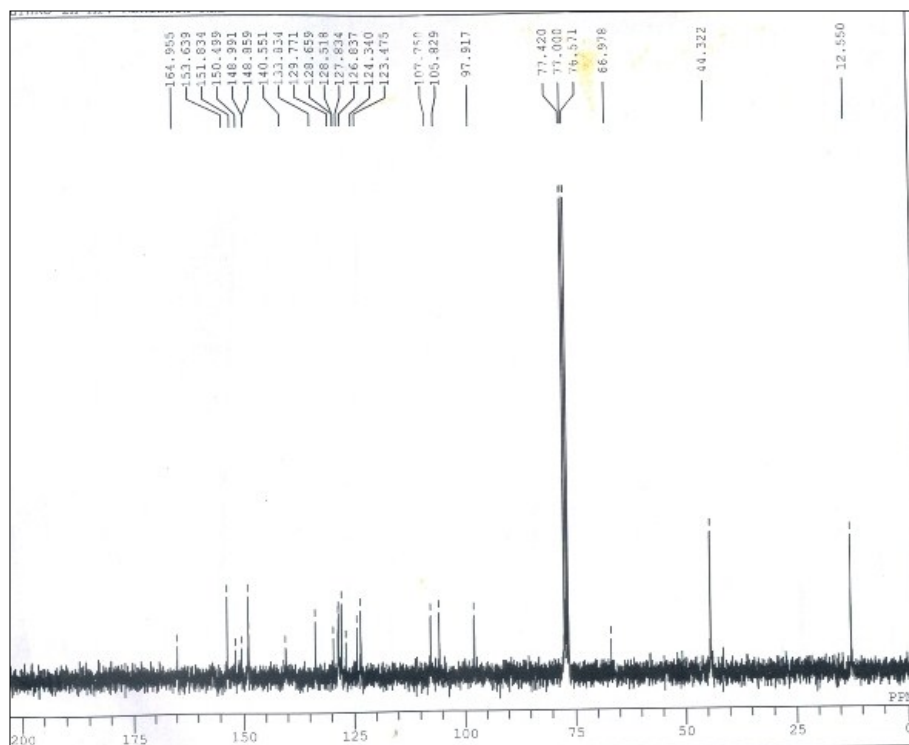


Fig. S2: ^{13}C -NMR spectrum of **RHTH** in CDCl_3 at room temperature

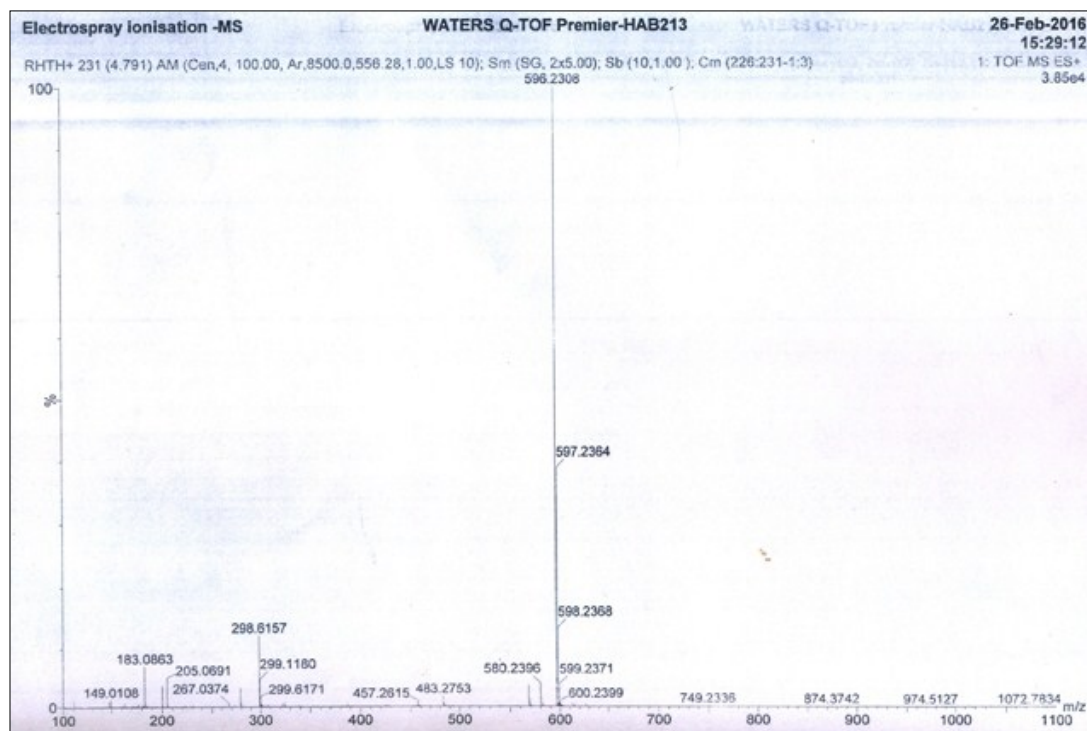


Fig. S3: ESI-MS spectrum of **RHTH**.

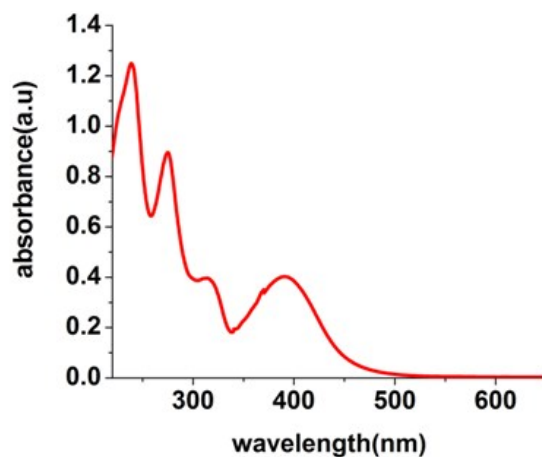


Fig. S4: UV-vis spectrum of **RHTH** (2.5×10^{-5} M, aqueous CH_3CN , 4:6, v/v, HEPES buffer, pH 7.2) at room temperature.

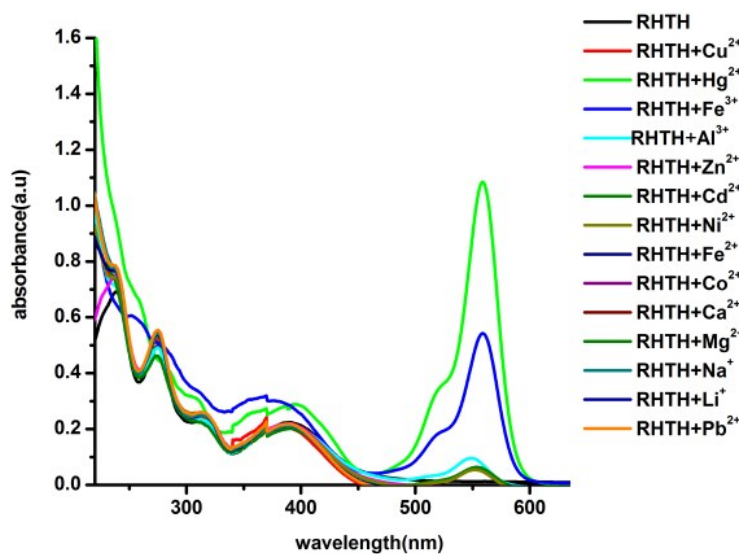


Fig. S5: UV-vis spectrum of **RHTH** (2.5×10^{-5} M, aqueous CH_3CN) upon titration with 2 equiv. of cations (Cu^{2+} , Hg^{2+} , Fe^{3+} , Al^{3+} , Zn^{2+} , Cd^{2+} , Ni^{2+} , Fe^{2+} , Co^{2+} , Ca^{2+} , Mg^{2+} , Na^+ , Li^+ and Pb^{2+}) in H_2O .



Fig. S6: Visual colour changes in the solution of **RHTH** ($2.5 \times 10^{-5} \text{M}$, aqueous CH_3CN (4:6, v/v, HEPES buffer, pH 7.2) on addition of 2 equiv. of different cations in H_2O . 1 = RHTH, 2 = RHTH + Ni^{2+} , 3 = RHTH + Fe^{2+} , 4 = RHTH + Hg^{2+} , 5 = RHTH + Li^+ , 6 = RHTH + Mg^{2+} , 7 = RHTH + Co^{2+} , 8 = RHTH + Fe^{3+} , 9 = RHTH + Cd^{2+} , 10 = RHTH + Pb^{2+} , 11 = RHTH + Ca^{2+} , 12 = RHTH + Cu^{2+})

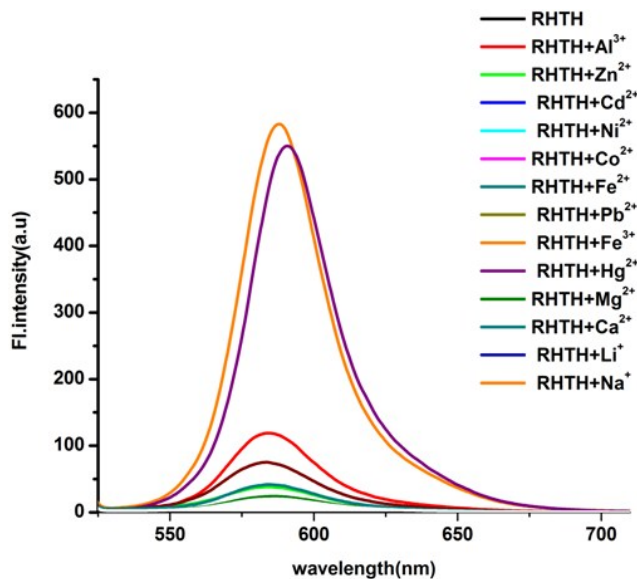


Fig. S7: Fluorescence spectrum of **RHTH** ($2.5 \times 10^{-5} \text{M}$) upon titration with 2 equiv. of cations (Cu^{2+} , Hg^{2+} , Fe^{3+} , Al^{3+} , Zn^{2+} , Cd^{2+} , Ni^{2+} , Fe^{2+} , Co^{2+} , Ca^{2+} , Mg^{2+} , Na^+ , Li^+ , Pb^{2+}) in H_2O .

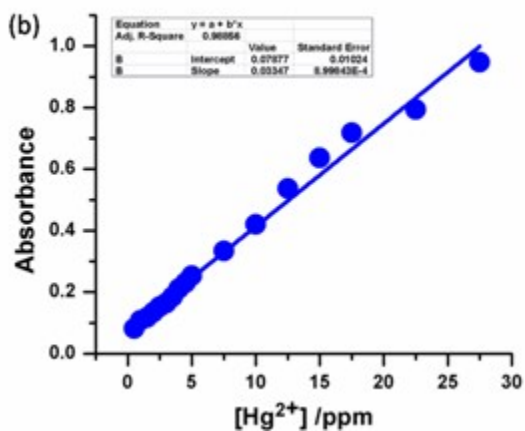
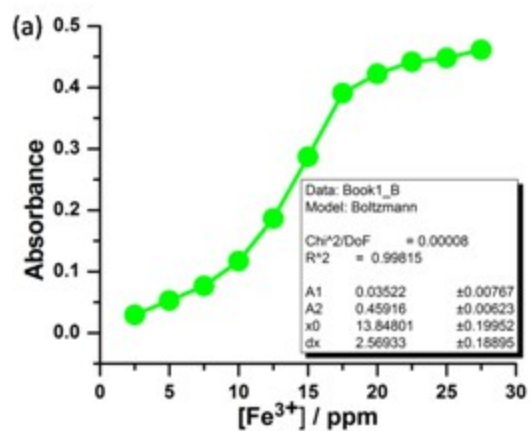
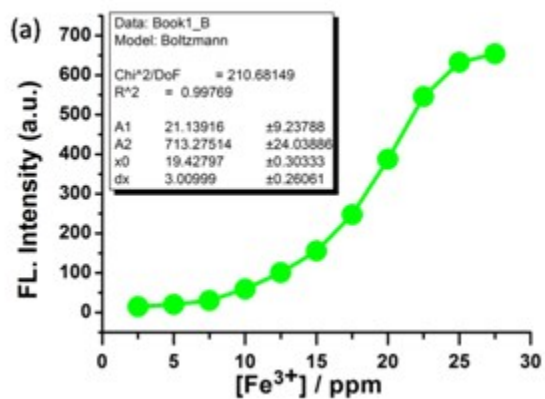


Fig. S8: Plot of absorbance at $\lambda_{\max} = 560$ nm as a function of ppm concentrations of (a) Fe^{3+} ($R^2 = 0.99$) and (b) Hg^{2+} ($R^2 = 0.98$) in H_2O .



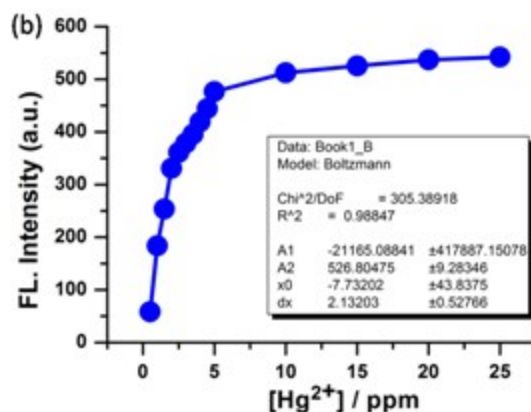


Fig. S9: Plot of fluorescence intensity (a) at $\lambda_{\max} = 587$ nm as a function of ppm level concentrations of Fe^{3+} in H_2O ($R^2 = 0.99$) and (b) at $\lambda_{\max} = 593$ nm as a function of ppm level concentrations of Hg^{2+} in H_2O ($R^2 = 0.98$).

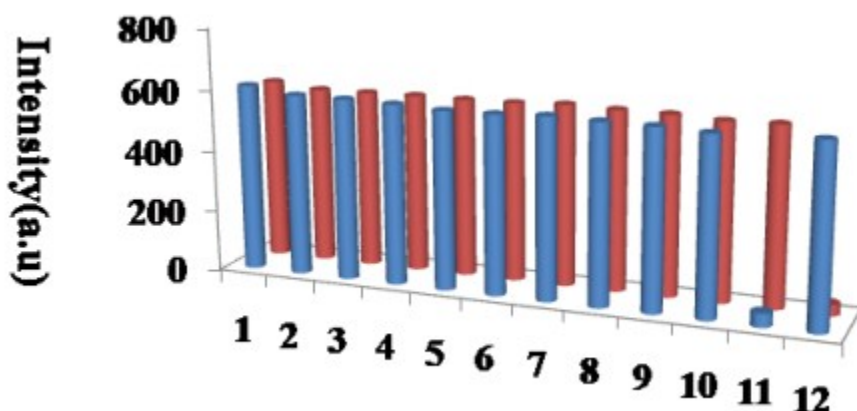


Fig. S10:(a) Representative bar chart showing intensity change at $\lambda_{\max} = 587$ nm on the addition of various anions (4 equiv. in H_2O) in the solution of **RHTH- Fe^{3+}** (1 equiv. of Fe^{3+} in 2.5×10^{-5} M, aqueous CH_3CN (4:6, v/v, HEPES buffer, pH 7.2 of **RHTH**, blue bars) and **RHTH- Hg^{2+}** (2 equiv. of Hg^{2+} in 2.5×10^{-5} M, aqueous CH_3CN (4:6, v/v, HEPES buffer, pH 7.2 of **RHTH**, red bars). 1 = None, 2 = AcO^- , 3 = NO_3^- , 4 = SCN^- , 5 = Br^- , 6 = HPO_4^{2-} , 7 = ClO_4^- , 8 = NO_2^- , 9 = I^- , 10 = Cl^- , 11 = CN^- , 12 = S^{2-} .

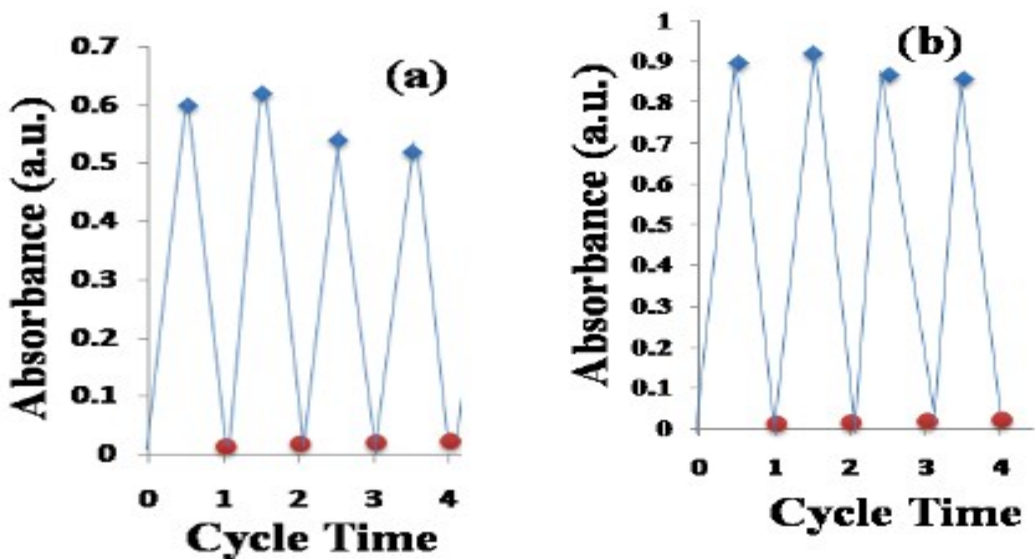


Fig. S11 Sensing-recovery cycles for **RHTH** at $\lambda_{\max} = 560$ nm (a) on the addition of Fe^{3+} (1 equiv.) (blue squares) and subsequent regeneration by CN^- (4 equiv.) and (b) upon addition of (1 equiv.) (blue squares) Hg^{2+} and subsequent regeneration by S^{2-} (2 equiv.).

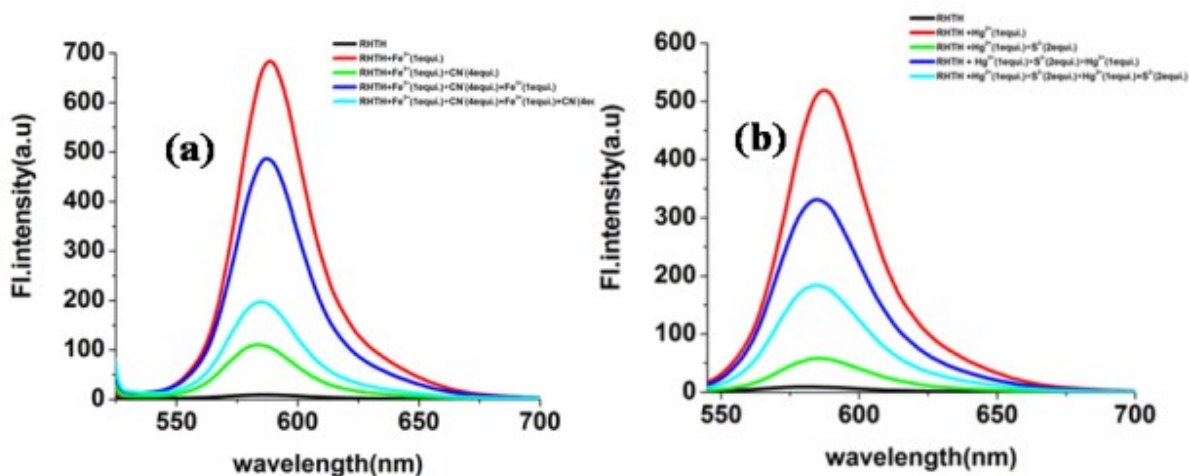


Fig. S12: Repeatability of **RHTH** evaluated by the alternative additions of (a) Fe^{3+} and CN^- ions (CN^- is 4 equiv. to Fe^{3+}) (b) Hg^{2+} and S^{2-} ions (S^{2-} is 2 equiv. to Hg^{2+}) alternately to the **RHTH** solution.

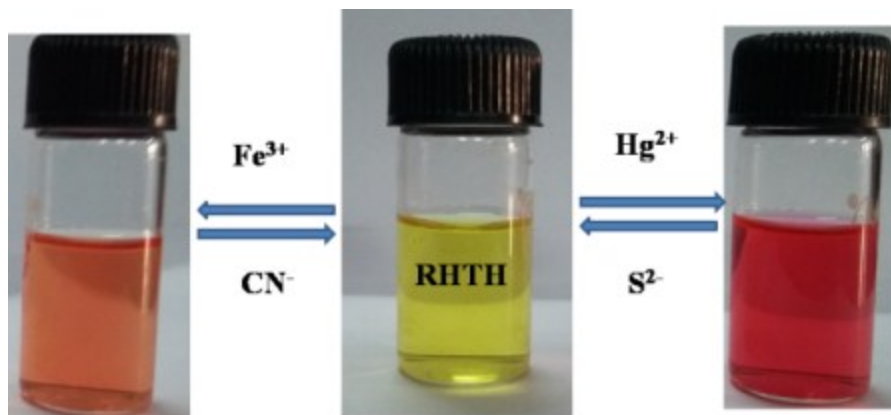


Fig. S13:Reversible visual colour changes in the solution of **RHTH**(10^{-4}M)

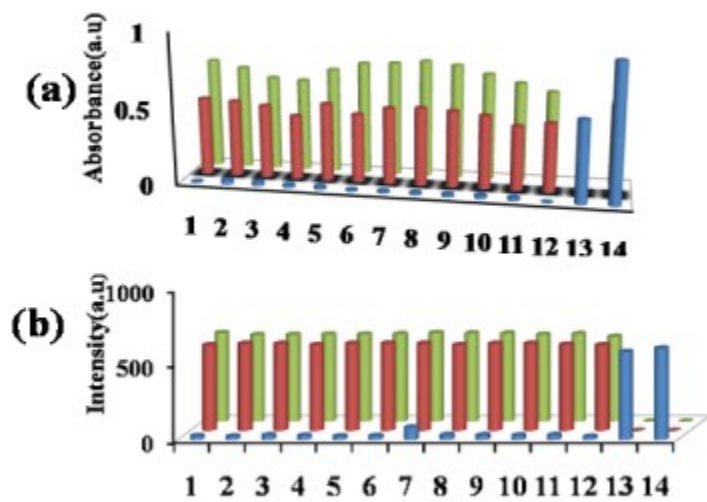


Fig. S14:Representative bar chart of **RHTH** ($2.5 \times 10^{-5}\text{M}$, aqueous CH_3CN (4:6, v/v, HEPES buffer, pH 7.2), on the addition of 5equiv. of various metal ions (blue bars). The red and olive green bars depict interference test of 5equiv. of Fe^{3+} and Hg^{2+} , respectively, in the presence of 5 equiv. of all other cations. 1 = Cd^{2+} , 2 = Zn^{2+} , 3 = Hg^{2+} , 4 = Li^+ , 5 = Cu^{2+} , 6 = Co^{2+} , 7 = Al^{3+} , 8 = Fe^{2+} , 9 = Pb^{2+} , 10 = Mg^{2+} , 11 = Na^+ , 12 = Ni^{2+} , 13 = Fe^{3+} , 14 = Hg^{2+} , (a) showing absorbance change at $\lambda_{\text{max}} = 560 \text{ nm}$ (b) intensity change at $\lambda_{\text{max}} = 587 \text{ nm}$.

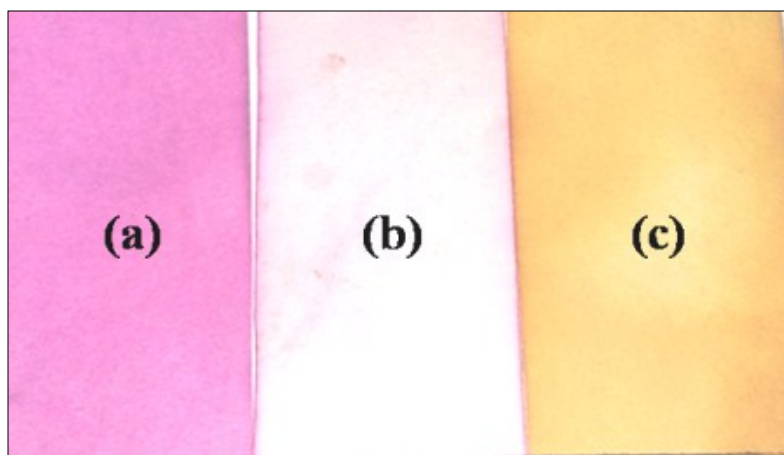


Fig. S15: Naked eye detection on a piece of paper soaked with **RHTH**: From left to right (a)**RHTH**+ Hg^{2+} ; (b)**RHTH** (blank) and (c)**RHTH** + Fe^{3+} . Test paper was soaked with **RHTH**, dried and then immersed in solution of Fe^{3+} and Hg^{2+} in H_2O .

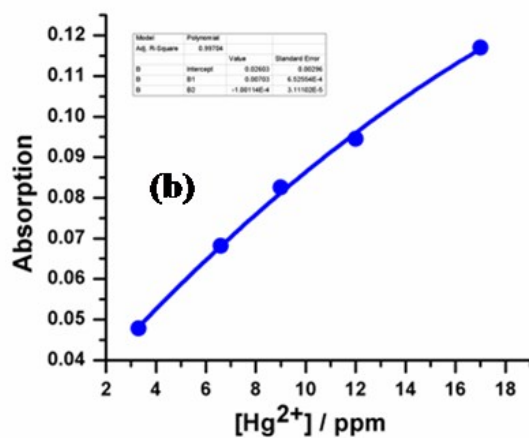
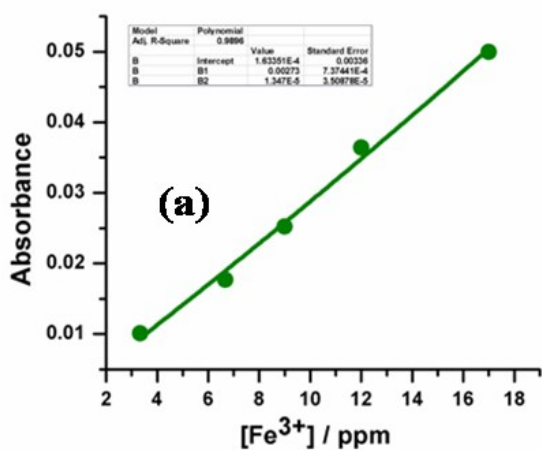


Fig. S16: Proof-of-concept experiments with **RHTH** (at $\lambda_{\text{max}} = 560 \text{ nm}$) for determining (a) Fe^{3+} ($R^2 = 0.98$) and (b) Hg^{2+} in tap water ($R^2 = 0.99$) solutions.

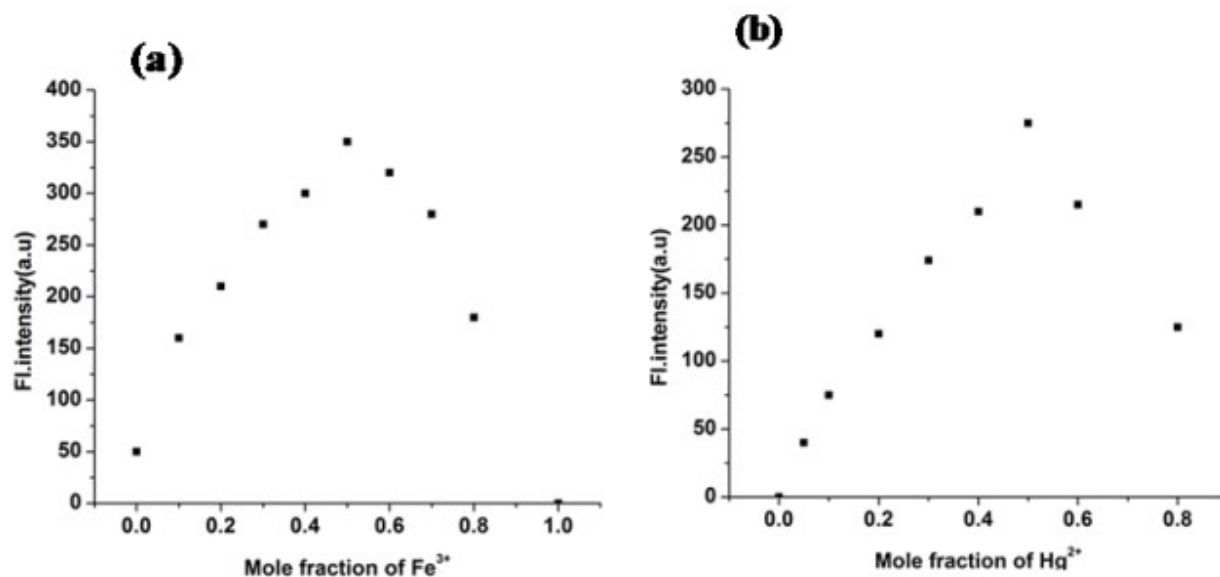


Fig. S17: Job's plot for varying mole-fraction at $\lambda_{\max} = 587\text{nm}$ (a) Fe³⁺ and (b) at $\lambda_{\max} = 593\text{nm}$ for Hg²⁺.

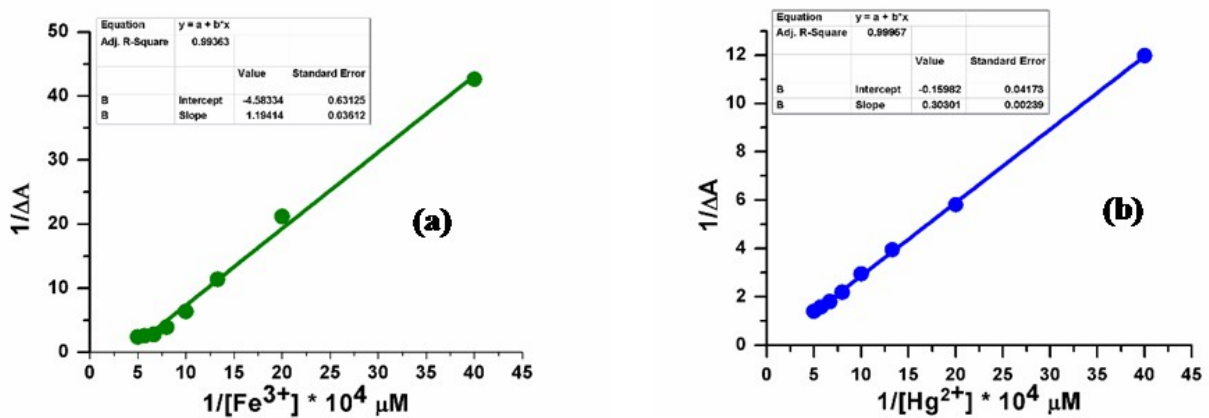


Fig. S18: Graph showing the variation of (a) $1/[\text{Fe}^{3+}]$ vs $1/\Delta A$ ($R^2 = 0.993$) and (b) $1/[\text{Hg}^{2+}]$ vs $1/\Delta A$ ($R^2 = 0.999$) used for the determination of binding constants.

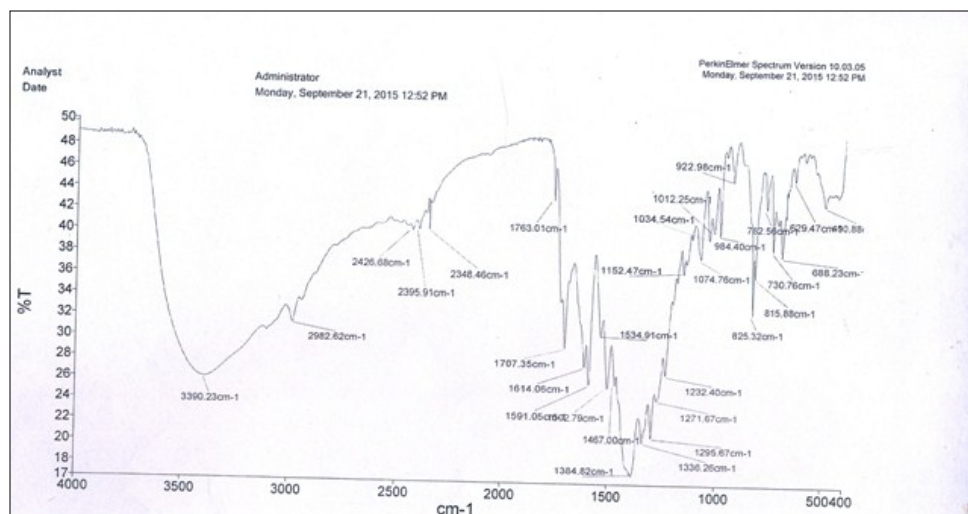


Fig S19: FTIR spectrum of [RHTH-Fe³⁺] complex .

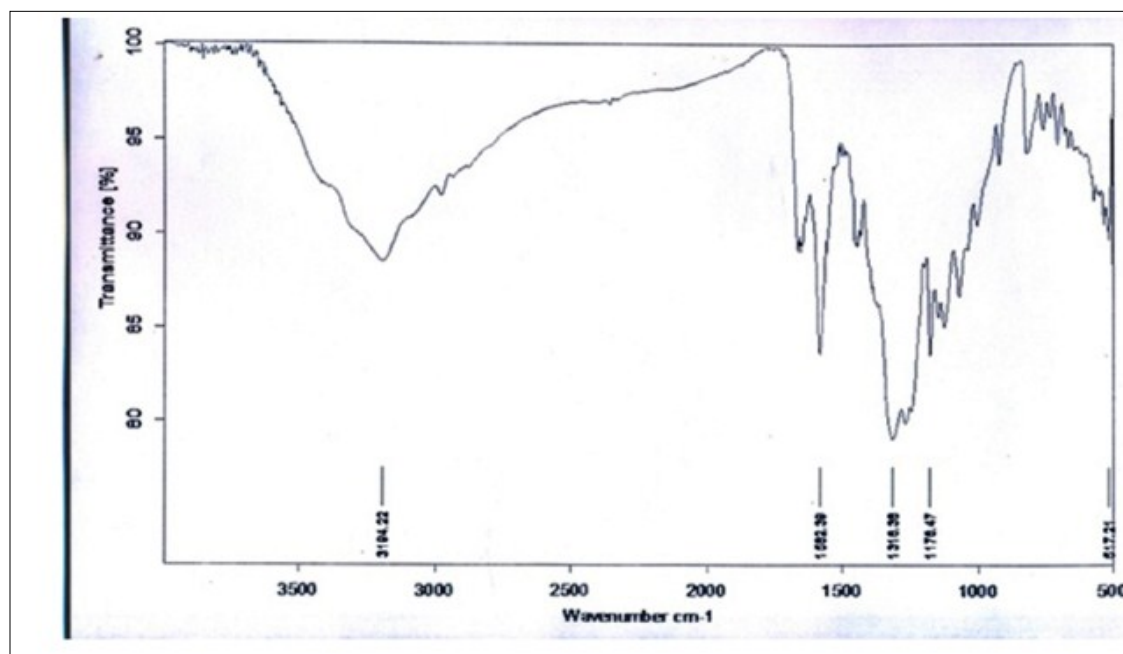


Fig S20: FTIR spectrum of the product formed after Hg²⁺ assisted hydrolysis of RHTH.

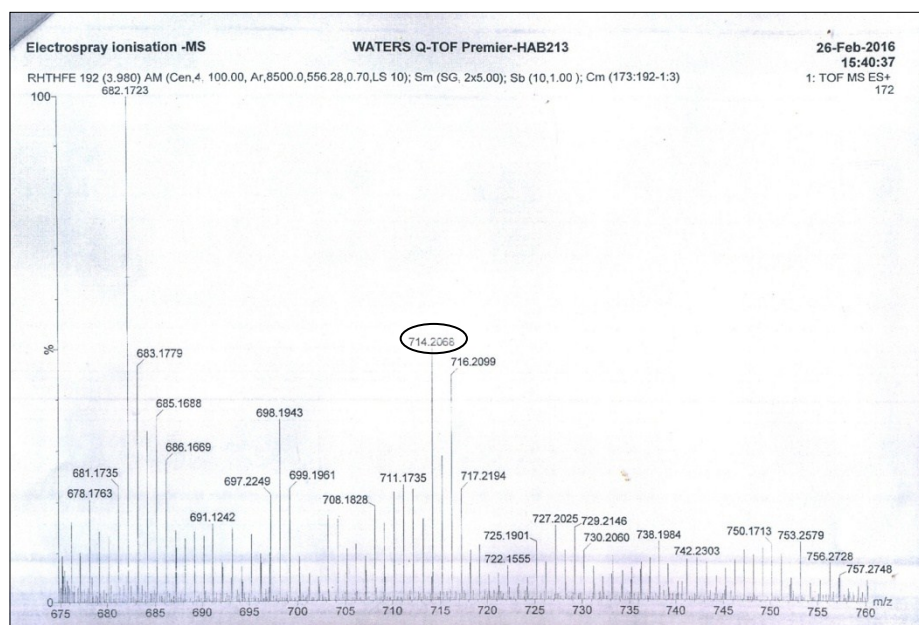


Fig.S21:ESI-MS spectrum of isolated solid[RHTH-Fe³⁺] complex.

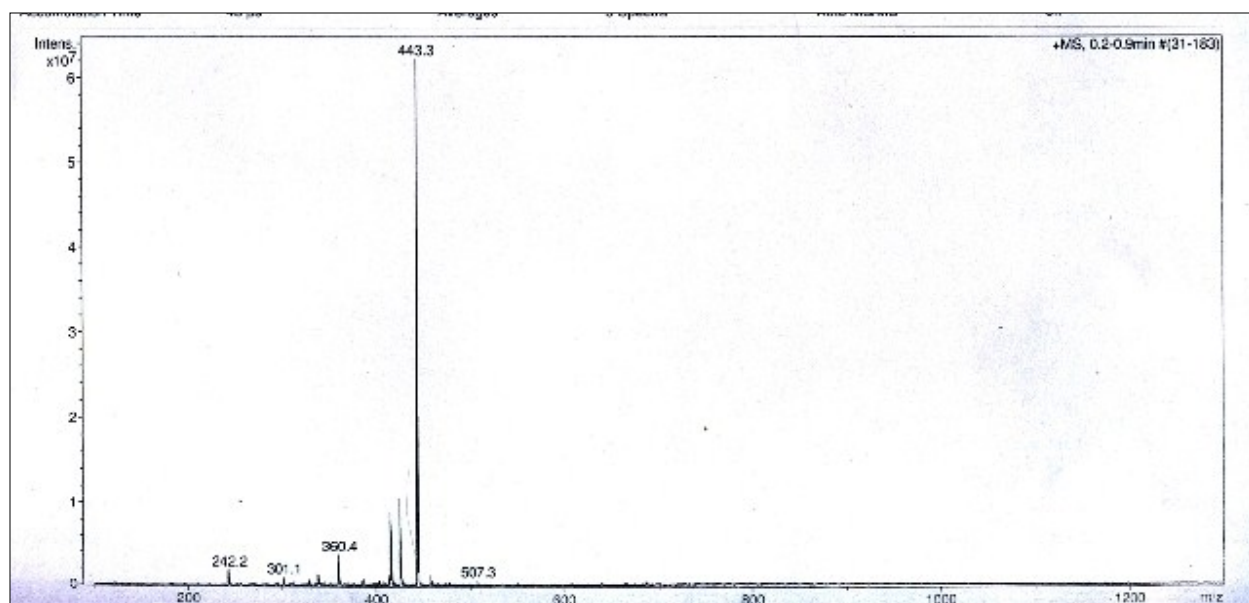


Fig.S22: ESI-MS spectrum of the product formed after Hg^{2+} assisted hydrolysis of **RHTH**.

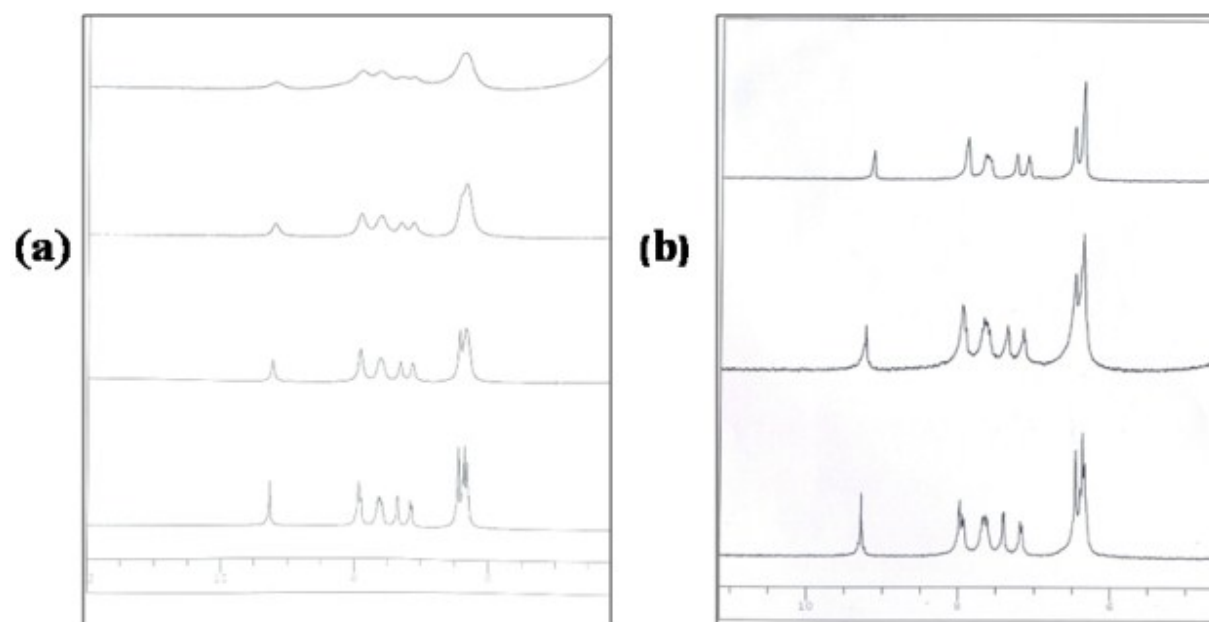


Fig.S23: Partial ^1H NMR spectra of titrations of **RHTH** in presence of (a) Fe^{3+} and (b) Hg^{2+} ions.

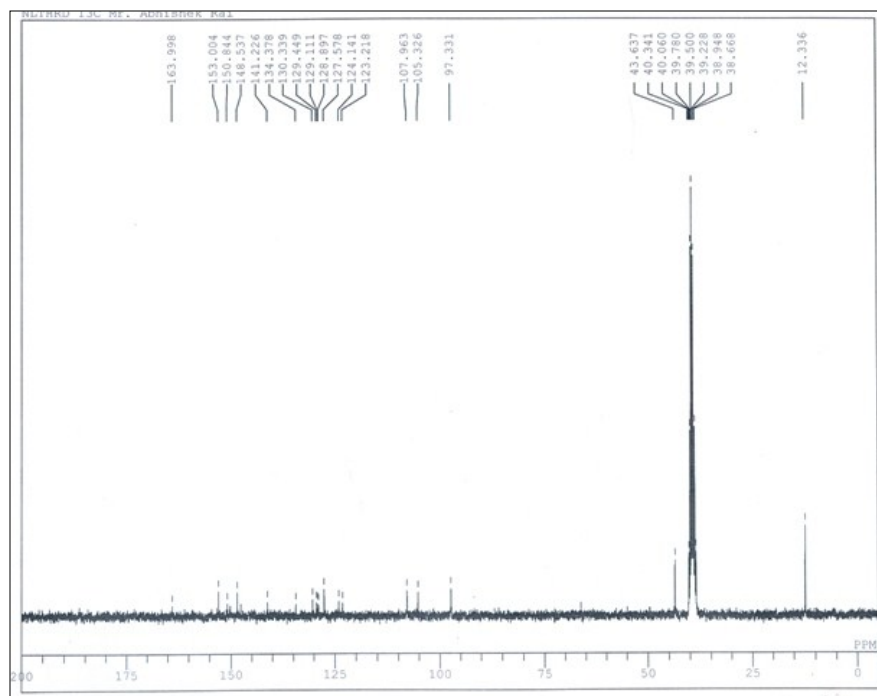


Fig.S24: ^{13}C NMR spectrum of $[\text{RHTH-Fe}^{3+}]$ complex .

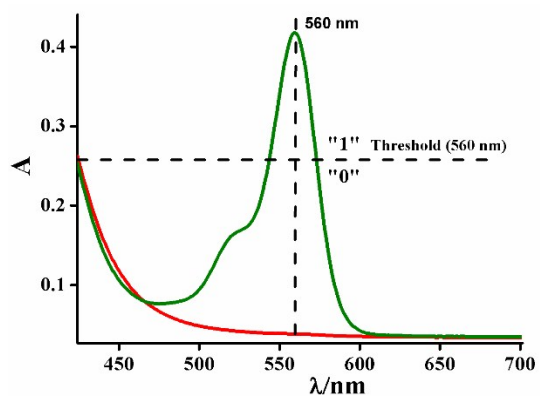


Fig. S25: Representative spectra showing the absorbance changes at $\lambda_{\max} = 560$ nm on the addition of Fe^{3+} (green) to the solution of **RHTH** (red). The 560 nm band has been used as the output in the logic circuit and the assumed threshold value has been clearly marked here. The absorbance more than the threshold values are assigned as “1” and absorbance lesser than the threshold values are assigned as “0” corresponding to the “on” and “off” states of the readout signals, respectively.

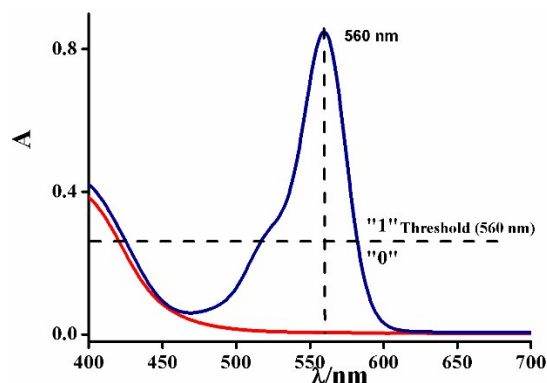


Fig. S26: Representative spectra showing the absorbance changes at $\lambda_{\max} = 560$ nm on the addition of Hg^{2+} (blue) to the solution of **RHTH** (red). The 560 nm band has been used as the output in the logic circuit and the assumed threshold value has been clearly marked here.

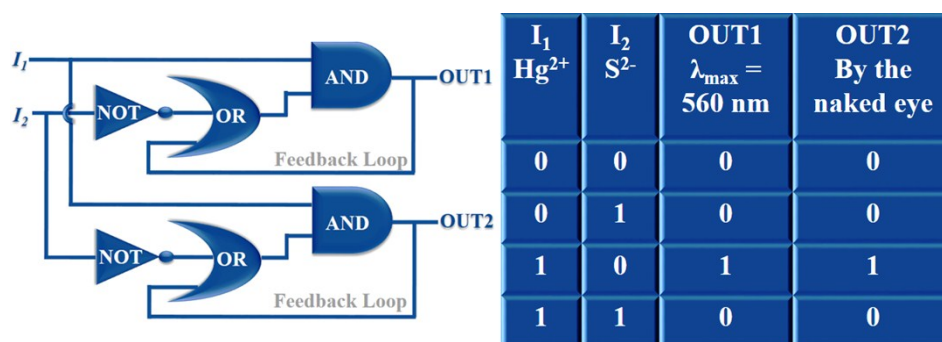


Fig. S27: Truth table and sequential logic circuits displaying memory units with two inputs and two outputs in the presence of chemical inputs *viz.* I_1 (Hg^{2+}) and I_2 (S^{2-}). The absorbance more than the threshold values are assigned as “1” and absorbance lesser than the threshold values are assigned as “0” corresponding to the “on” and “off” states of the readout signals, respectively. The colour change from yellow to magenta colour is allocated as “0” and “1” respectively.

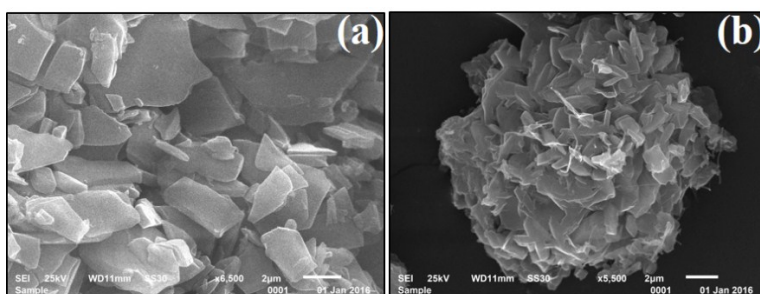


Fig. S28:SEM images of **RHTH** (a) in the state of as-prepared solid and (b) after grinding.

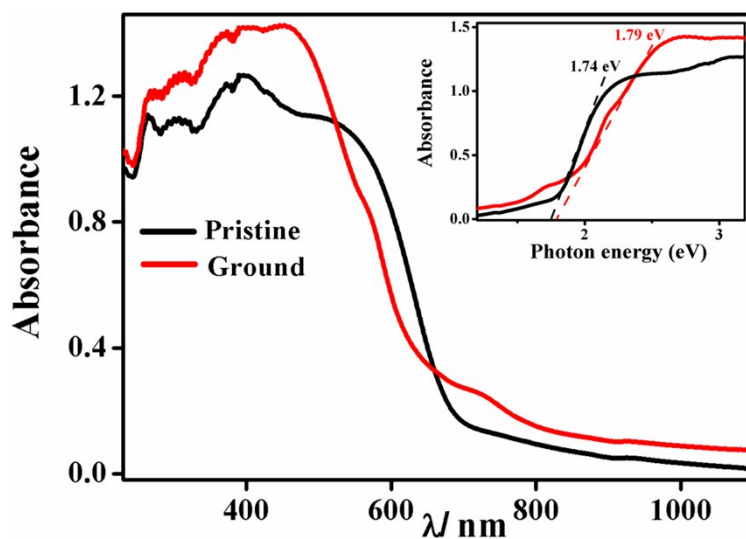


Fig. S29:UV-Vis diffuse reflectance spectra of **RHTH** in the state of as-prepared solid (black) and after grinding (red). Inset shows the bandgap estimation using the Kubelka–Munk function.

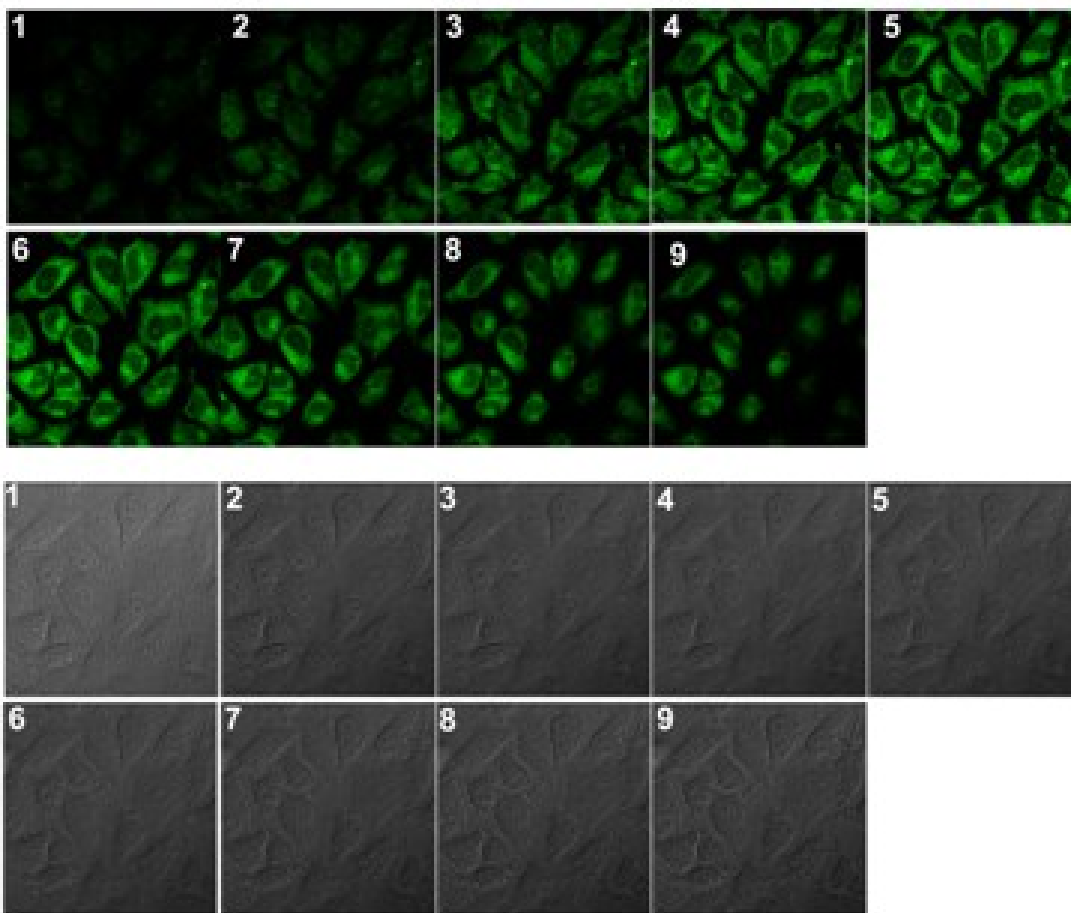


Fig. S30:MCT images of HeLa cells supplemented with 10 μM MRHTH In the presence of 100 μM Hg^{2+} for 1 h at 37 $^{\circ}\text{C}$.

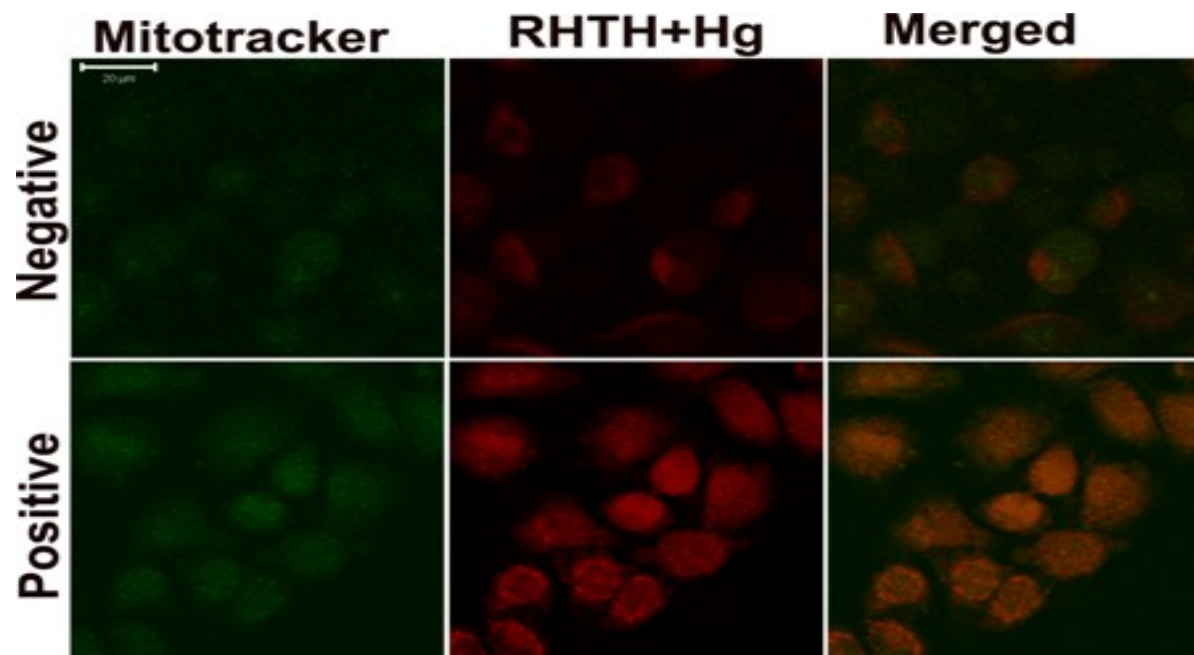


Fig. S31:Subcellular localization of **RHTH**,MitoTracker is used. MitoTracker selectively stain mitochondria. The fluroscent signal of **RHTH** and MitoTracker is found to be colocalized that suggests **RHTH** may have mitochondrial localization.